Scripta Materialia xxx (2015) xxx–xxx

Contents lists available at ScienceDirect

Scripta Materialia

journal homepage: www.elsevier.com/locate/scriptamat

Helium bubble evolution in ion irradiated Al/B_4C metal metrix composite

Feifei Zhang [a,b], Xu Wang [a,b], Jonathan B. Wierschke [a], Lumin Wang [b,a,*]

[a] College of Energy, Xiamen University, Xiamen, Fujian 361102, China
[b] Department of Nuclear Engineering and Radiological Science, University of Michigan, Ann Arbor, MI 48109, United States

ARTICLE INFO

Article history:
Received 8 April 2015
Revised 2 July 2015
Accepted 5 July 2015
Available online xxxx

Keywords:
Interface defects
Ceramics
Metal matrix composites
Transmission electron microscopy
Helium bubble

ABSTRACT

Helium behavior in Al/B_4C metal matrix composite with two different sets of ion irradiation conditions has been investigated by transmission electron microscopy. Helium bubbles in Al were found to be much larger than those in B_4C after a helium fluence of 1.5×10^{17} ions/cm^2 at the room temperature. Also, bubbles at grain boundaries and their vicinity in aluminum are faceted. With additional proton irradiation, a bubble denuded zone along the aluminum grain boundary appears. The results are discussed in terms of the energetics of the material system.

Al/B_4C metal matrix composite (MMC) is an important neutron absorbing material used in both wet storage pools and dry storage casks of spent nuclear fuel for preventing criticality. Al/B_4C MMC can effectively absorb fast and thermal neutrons, because of the high neutron absorption cross-section of ^{10}B through the $^{10}B(n, \alpha)^7Li$ transmutation reaction for a wide energy range of neutrons.

The damage produced by elastic collisions between neutrons and other energetic particles generated by transmutation reactions with the target atoms along with the build-up of helium concentration in the MMC may lead to the precipitation of helium bubbles. The gamma and neutron doses received in the MMC depend on a number of factors including fuel burnup, storage time, and the self-shielding of the fuel assemblies. In spent fuel fool storage, the neutron flux can be as high as 2.6×10^5 neutron/cm^2 s and the gamma dose rate is in the range of 0.1–10 kGy/h [1,2], corresponding to several thousand appm of transmuted helium build up and 1–2 dpa (displacement per atom) of damage during the estimated storage period of 60 years in spent fuel pool storage and about 200 years in the dry storage casks.

As a control rod material, the defect structure in neutron irradiated B_4C was investigated by Ashbee [3,4], Jostsons [5,6], Hollenberg [7] and Donomae [8] et al. He^+ implantation of B_4C has been performed by Stoto [9] and Maruyama [10]. Irradiation effects and helium bubble formation in aluminum after high energy proton irradiation were reported by Singh and Victoria [11,12]. The precipitation of helium causes not only changes in microstructure but degradation in the physical, chemical and mechanical properties of Al/B_4C MMC, such as, reduced thermal conductivity, decreased corrosion resistance and volume swelling. The property change in Al/B_4C MMC affects the long-term performance of the MMC in its working environment. In fact, irradiation induced microcracking in B_4C that leads to increased boron release was reported by Copeland [13] and Stoto [14].

This paper focuses on helium bubble formation upon helium implantation and bubble evolution during additional proton irradiation in the Al/B_4C MMC. Ion irradiations were conducted to simulate the effects of radiation and helium build-up in Al/B_4C MMC as neutron absorbers in wet storage pool and dry storage casks. Angular shape B_4C particles with an average particle size of 10 μm were used in the Al/B_4C MMC.

Two different sets of ion irradiation experiments were carried out to simulate the effects of helium accumulation and irradiation damage in the MMC used in both wet and dry spent nuclear fuel storage facilities. Parameters of the two-irradiation conditions, *Irradiation A* and *Irradiation B*, are listed in Table 1.

Irradiation A is a sole He^+ irradiation where a bulk MMC sample was implanted with 400 keV He^+ to 1.5×10^{17} ions/cm^2 at room temperature (RT). The SRIM (the Stopping and Range of Ions in Matter) code has been used to calculate both helium concentration

* Corresponding author at: Department of Nuclear Engineering and Radiological Science, University of Michigan, Ann Arbor, MI 48109, United States.
E-mail address: lmwang@umich.edu (L. Wang).

http://dx.doi.org/10.1016/j.scriptamat.2015.07.011
1359-6462/

Table 1
Two sets of ion irradiations.

	Ions	Fluence (ions/cm^2)	Irradiation direction
Irradiation A	400 keV He^+	1.5×10^{17}	→
Irradiation B	400 keV He^+	1.0×10^{16}	→
	1.5 MeV H^+	2.2×10^{19}	↓

and damage production after the irradiation. Fig. 1a shows the SRIM results overlapped on a typical TEM micrograph of MMC specimens after *Irradiation A*.

Irradiation B includes a pre-implantation of 400 keV He^+ to 1.0×10^{16} ions/cm^2 followed by a 1.5 MeV proton irradiation to 2.2×10^{19} ions/cm^2 in the perpendicular direction to the helium beam, as shown in Fig. 1b. The area suffered with both He^+ pre-implantation and proton irradiation was marked in light blue in Fig. 1b. Although all irradiations were conducted at RT, temperature of the sample surface reached 110 ± 10 °C due to beam heating during proton irradiation, as indicated by an infrared thermometer. Both helium implantation and proton irradiation were carried out at the Michigan Ion Beam Laboratory.

According to the SRIM simulation results, helium concentration and displacement damage reached as high as 10 at.% and 3–5 dpa, respectively, after *Irradiation A*, much higher than what would be achieved in the spent nuclear fuel storage facilities. In *Irradiation B*, the helium concentration is about 0.7 at.% at the peak helium depth, which is close to the real accumulated helium concentration in the spent fuel storage facilities. Fig. 1c is the SRIM results for 1.5 MeV proton irradiation. A depth range with about 1 dpa damage due to proton irradiation but little hydrogen introduction was selected for TEM analysis. Radiation damage generated by the He^+ implantation in the same region of the sample is less than 0.3 dpa. So the total radiation damage of selected area is 1–1.3 dpa, which matches the real operation condition of the material (1–2 dpa).

In order to investigate the depth distribution of helium bubbles and radiation-induced defects, cross-sectional TEM samples were prepared using the Focus Ion Beam (FIB) lift-out techniques. Fig. 1b shows the scheme of *Irradiation B*. A TEM sample was lifted-out from the He^+ irradiated surface with the sample plane parallel to the helium ion direction and including an overlap of He^+ implantation and proton irradiation. TEM analysis was conducted with a JEOL JEM3011 microscope at the Electron Microbeam Analysis Laboratory, University of Michigan.

TEM results of helium bubble evolution with different helium concentrations in the aluminum matrix were shown in Fig. 2. Fig. 2a–c were taken from the sample after *Irradiation B*, and the Fig. 2d was taken from the sample after *Irradiation A*. Without implanted helium, only a few voids (vacancy clusters) were observed (Fig. 2a). In the region with helium concentration from several hundred to several thousand appm, both density and size of helium bubbles increased in the Al grain with helium concentration (Fig. 2b and c). Larger bubbles along the Al grain boundaries were observed while the helium concentration reached several thousand appm (Fig. 2c). On average, bubbles on the aluminum grain boundaries are ~5 nm in diameter while those in the aluminum matrix are only ~3 nm in diameter. After *Irradiation A*, helium concentration is about 10 at.% (10^5 appm) at the peak depth

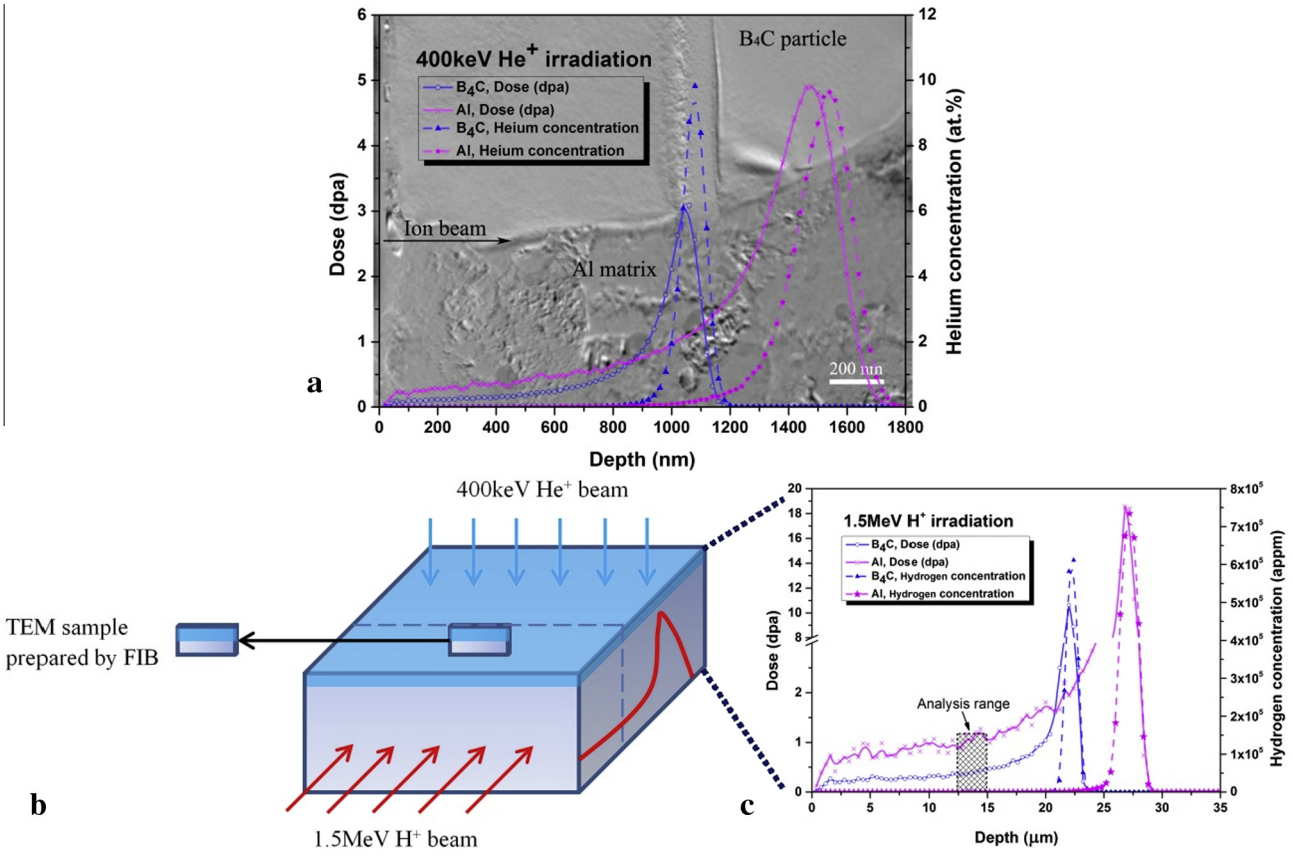

Fig. 1. (a) The damage distribution and He concentration of 400 keV He^+ irradiation (with fluence to 1.5×10^{17} ions/cm^2) predicted by SRIM and overlapped with an TEM micrograph, *Irradiation A*. (b) Scheme of *Irradiation B* and TEM sample preparation by FIB. The area suffered with both He^+ pre-implantation and proton irradiation was marked as light blue. (c) SRIM results of the damage distribution and H concentration irradiated by 1.5 MeV proton to 2.2×10^{19} ions/cm^2. (For interpretation of the references to colour in this figure legend, the reader is referred to the web version of this article.)

Please cite this article in press as: F. Zhang et al., Scripta Mater. (2015), http://dx.doi.org/10.1016/j.scriptamat.2015.07.011

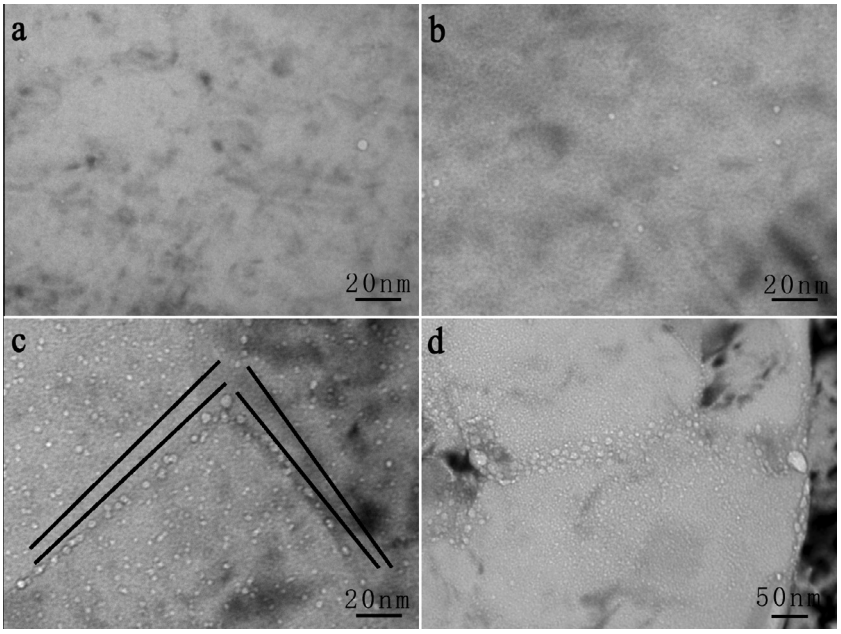

Fig. 2. Helium bubbles in Al matrix with increasing helium concentrations, (a) 0 appm, (b) 10^2 appm, (c) 10^3 appm, (d) 10^5 appm. (a)–(c) were taken from the sample after *Irradiation B*, and (d) was taken after *Irradiation A*. Bubble denuded zone with width of ~10 nm is visible and outlined in black in (c). The scale bar in (d) is different from (a–c).

range, and helium bubbles there grew to much larger sizes, especially on the grain and phase boundaries (10–25 nm in diameters), as shown in Fig. 2d.

In the spent nuclear fuel storage pool, the MMC is surrounded by water. At the end of spent fuel pool storage, the fuel assembly would be transferred to the dry storage cask. Small amount of residual water may stay in the cask. For long time storage, the helium builds up by $^{10}B(n,\alpha)^7Li$ reaction, and helium bubble growth and coalescence will accelerate oxygen diffusion through grain/phase boundaries. With the increasing helium concentration, the large helium bubbles along the grain and phase boundaries tend to coalesce to a channel, leading the inner B_4C particles to interact with water during spent fuel storage. The results of accelerated corrosion tests on ion irradiated samples indicate that the inner boron carbide particles were lost through open channels along the grain boundaries and phase boundaries [15].

A denuded zone of helium bubbles along the aluminum grain boundaries is visible after *irradiation B* while it was not observed in *irradiation A*. The bubble denuded zone is apparently dependent on the helium concentration and irradiation temperature. After the proton irradiation, the values of bubble density and diameter in aluminum matrix follow the general trends of bubble evolution according to existing theories. Atomic displacements and the resulting vacancies, self-interstitial atoms (SIAs) and clusters of these defects play important role on helium diffusion. During proton irradiation, temperature of the sample surface reached 110 °C due to the ion beam heating. This temperature is about $0.2T_m$ for aluminum. At this temperature, the following mechanisms should be considered, "displacement mechanism" where helium diffusion is due to direct displacements and "replacement mechanism" where a helium atom diffuses interstitially between its replacement from vacancy by a self interstitial atom and its re-trapping by another vacancy [16]. At high helium concentration, helium resolved from small bubbles by displacement cascade may result in secondary nucleation of bubbles. The process of secondary nucleation enhances helium diffusion, leading to bubble segregation to certain pre-existing defects. A grain boundary can attract helium atoms from a relatively large volume of material, so the bubble denuded zone along the boundaries was visible after *irradiation B*. Dauben presented a similar result on irradiated Fe–Cr alloy with pre-implanted helium [17].

The transformation of helium bubbles in B_4C is an anomaly. After *Irradiation A*, a band of a high density of small helium bubbles centered at the peak helium concentration depth was observed in B_4C (Fig. 3a). These small helium bubbles, about 1 nm in diameter on average, were homogeneously distributed throughout the band in B_4C. In addition to the contrasts of helium bubbles, a number of black dots were observed at the damage peak range in B_4C. These black dots are thought to be the contrasts produced by radiation induced dislocation loops.

After *Irradiation B*, helium bubbles arranged in rows, about 5 nm in diameter, were observed in the B_4C. These bubble strings were arranged in several directions (Fig. 3d and e), presumably on pre-existing defect. Previous works have shown that lined up or orientated helium bubbles can form during high temperature neutron irradiation or after high temperature annealing [6–8]. Helium bubble strings were seen when B_4C was irradiated by 16 MeV He^+ at a much higher temperature (1720 °C) by Stoto [9]. Compared to the high melting point of B_4C (T_m = 3036 K), our experiments were conducted at a relatively low temperature. At low temperatures ($<0.2T_m$), the "displacement or cascade mixing mechanism" where helium diffuses is due to direct displacements shall dominate [16]. The nuclei collision induced damage by proton irradiation alone is 1 dpa. Although the damage peak in B_4C is ~3 dpa (Fig. 1a) after the He^+ irradiation in *Irradiation A*, the size of helium bubbles in B_4C was only about 1 nm in diameter. The SRIM calculations show that the energy deposition due to ionization of *Irradiation B* is two orders of magnitude higher than that of *Irradiation A*. Inui reported boron carbide and many other ceramics can be affected by electron irradiation [18–20]. The covalent and ionic bonds in B_4C, may be susceptible to ionization induced radiation damage. Since ionization may induce substantial displacements and enhance helium diffusion in B_4C, its effect cannot be neglected.

The pre-existing defects may act as strong traps for the mobile helium atoms. The helium bubble strings are promoted by ionization and nuclei displacement damages that cause the helium atoms to move to pre-existing defects. Clusters of helium bubbles were found to be distributed heterogeneously within the B_4C grains.

Please cite this article in press as: F. Zhang et al., Scripta Mater. (2015), http://dx.doi.org/10.1016/j.scriptamat.2015.07.011

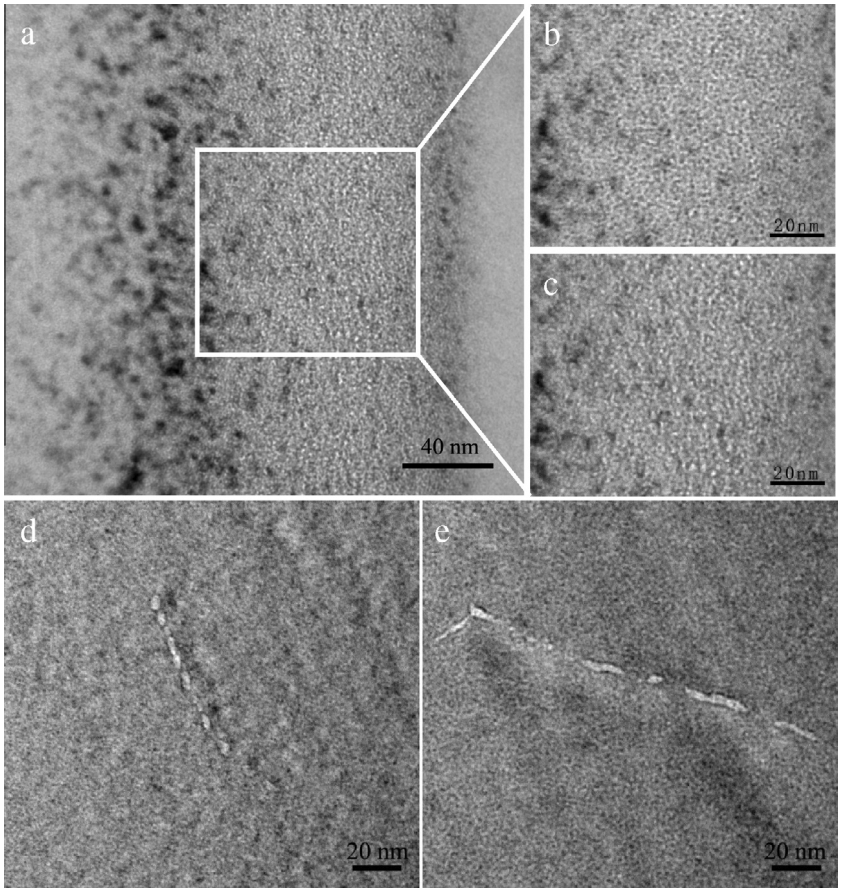

Fig. 3. (a) Under focus bright-field TEM micrograph showing the peak helium range of B_4C after *Irradiation A*, (b) Over- and (c) under-focused TEM images at higher magnification. (d and e) Helium bubbles lined-up in B_4C, after *Irradiation B*.

Coalescence of helium bubbles into strings may lead to the formation of short microcracks [9].

The sizes of helium bubbles are significantly different between aluminum and B_4C after *Irradiation A*. The state of helium contained in a bubble is defined by the gas density state and its corresponding pressure. For possible values of the pressure inside a bubble, two distinctly different limiting cases were presented [16]:

(1) The limit of mechanical stability of the matrix yields spontaneous plastic deformation. Calculations have shown that corresponding upper bound limit of the pressure may be reasonably represented by [21]

$$p \leqslant 0.2\mu \tag{1}$$

where μ is the shear modulus of the matrix.

At high helium to dpa ratio, the number of available helium atoms dominates the bubble evolution since most of the concurrently produced self-interstitial atoms (SIAs) and vacancies are annihilated at existing bubbles [16], it is likely that the pressure is close to the limit given by Eq. (1). For B_4C and aluminum, where $\mu \approx 200$ GPa and 26 GPa, the mechanical limits are as high as 40 GPa and as low as 5 GPa, respectively. That alone can explain the difficulty for the bubble growth in B_4C than in aluminum.

(2) The condition of thermodynamic equilibrium yields

$$p = 2\gamma/R \tag{2}$$

where γ is the surface energy and R is average bubble radius.

The pressure p can be described by the ideal gas equation for spherical bubbles:

$$\frac{4}{3}\pi R^3 p = nkT \tag{3}$$

where n is the number of helium atoms contained in a bubble, k is Boltzmann constant, T is thermodynamic temperature. Eqs. (2) and (3) lead to the number of helium atoms contained in a bubble of radius R:

$$n = \frac{8}{3}\frac{\gamma}{KT}\pi R^2 \tag{4}$$

The number of atomic sites, N, contained in the bubble is [9]

$$N = \frac{4}{3}\pi R^3 \rho_{at} \tag{5}$$

where ρ_{at} is the atomic density. The ratio of n/N can be represented as:

$$\frac{n}{N} = \frac{2\gamma}{kT\rho_{at}R} \tag{6}$$

At the peak helium range, helium concentrations in B_4C and aluminum matrix are similar. Based on Eq. (6), the size of helium bubbles in aluminum should be larger than those in B_4C with the same n/N value under the thermodynamic equilibrium condition. The difference in the bubble size between the two materials can be viewed as the result of the ideal gas law. As observed in our experiment, the average size of helium bubbles in aluminum and B_4C are 5 nm and 1 nm in diameter, respectively.

Please cite this article in press as: F. Zhang et al., Scripta Mater. (2015), http://dx.doi.org/10.1016/j.scriptamat.2015.07.011

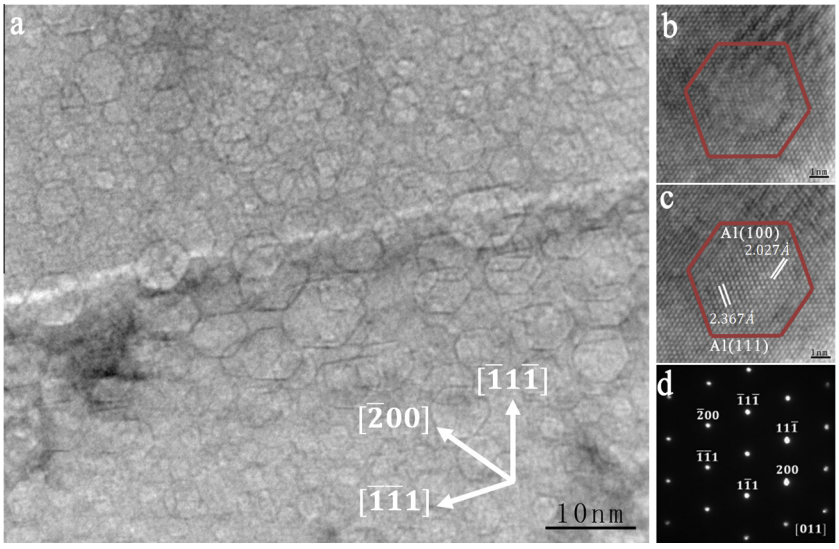

Fig. 4. (a) TEM images showing preferential orientations for faceted bubbles grown in Al after *Irradiation A*. Through-focus HRTEM images (b and c) show contrast of a faceted bubble in the nether Al grain of (a). (d) is SAED pattern of the nether Al grain of (a).

The small nano-scale bubbles could withstand very high helium concentrations and bubble inner pressures. For instance, in B_4C where $\gamma \approx 1.0 \times 10^3$ ergs/cm^2 [9], the equilibrium pressure reaches values of ~4 GPa, according to Eq. (2) when $R = 0.5$ nm. Compared with the Al {1 1 1} planes, where $\gamma < 1.0 \times 10^3$ ergs/cm^2 [22–24], the equilibrium pressure is less than 1 GPa when $R = 2.5$ nm. Considering the higher bonding energy of covalent bond and ionic bond in B_4C that corresponds to the high mechanical limit (~40 GPa), the smaller size bubbles in B_4C can withstand higher bubble pressure than in aluminum.

After *irradiation A*, at the shallower side of the helium peak region, faceted bubbles along a grain boundary were observed (Fig. 4a). The through-focus sequences of HRTEM images in Fig. 4b and c show contrast between the aluminum matrix and a faceted bubble in the lower aluminum grain of Fig. 4a. The hexagon bubbles are seen in ⟨1 1 0⟩ projection with {1 1 1} (d = 2.367 Å) and {1 0 0} (d = 2.027 Å) planes of aluminum normal to the plane of the image, based on the analyses of HRTEM images and SAED pattern (Fig. 4d). In order to minimize the overall free energy, the bubbles need to preferentially rearrange its surface via surface diffusion during their growth, and the facets with lowest surface energy planes will occupy most of the surface [25,26]. In the fcc structure, the lowest surface energy is found on the most closely packed {1 1 1} planes. Nelson has determined the surface energy sequence for aluminum is $E(1\,1\,1) < E(1\,0\,0) < E(1\,1\,0)$ [27]. In our case, {1 0 0} planes occupy two corners of the octahedral composed of {1 1 1} planes. The total surface area of a faceted bubble with the {1 1 1} surfaces is decreasing when the bubble is truncated by the {1 0 0} planes. A truncated octahedron or rounded corners are more energetically favorable. Since it is embedded in the substrate and consists of {1 1 1} planes, the octahedron has the same symmetry as that in the substrate. The faceted cavities with fluid/solid Xe were reported by Donnelly [28]. Cavities are generally observed to be tetra-decahedral in shape, that is a {1 1 1} octahedral with six {1 0 0} truncation [29]. As seen in Fig. 4a, the faceted bubbles at grain boundary are not perfect. The imperfect octahedral bubbles will be formed under the influence of defects because the diffusivities are higher along dislocation lines or grain boundaries [25].

Helium bubbles formed in aluminum matrix at a wide range of helium concentrations. The density and size of helium bubbles increased with increasing helium concentration. The bubbles formed on grain boundaries and phase boundaries are, on average, larger than those in the aluminum matrix. Helium bubbles in boron carbide were only observed at the helium peak range, and are much smaller in size. The intrinsic properties, such as strong covalent and ionic bonds and high shear modulus, cause the high pressure tolerance of helium bubbles in boron carbide that inhibits the bubble growth. Mechanisms of helium diffusion and bubble nucleation explain the bubble evolution under the 1.5 MeV proton irradiation. A bubble denuded zone along the grain boundary was visible due to "displacement mechanism" and "replacement mechanism", leading to helium atoms diffusion. The grain boundary re-trapped helium atoms around it. In boron carbide, helium bubbles grew to ~5 nm in diameter and lined-up along pre-existing defects after *Irradiation B*. These processes were controlled by the cascade induced helium dissolution, secondary bubble nucleation, and "displacement mechanism" of helium diffusion. Both nuclei collision and ionization induced secondary displacement promote the helium atom diffusion thus bubble nucleation and growth. Faceted bubbles were observed at grain boundaries and the nearby area in aluminum. These faceted bubbles consist of the {1 1 1} and {1 0 0} planes as their surfaces, which is the most energetically favorable configuration.

Acknowledgements

This work has been supported by the US DOE NEUP Program under the contract No. DE-AC07-05ID14517. Feifei Zhang also acknowledges the financial support from the China Scholarship Council.

References

[1] L. Lakosi, C. Tam Nguyen, Nucl. Instrum. Methods Phys. Res. B 580 (2007) 788.
[2] N.C. Tam, L. Lakosi, Radiat. Meas. 34 (2001) 601.
[3] K.H.G. Ashbee, Acta Metall. 19 (1971) 1079.
[4] K.H.G. Ashbee, C.K.H. Dubose, Acta Metall. 20 (1972) 241.
[5] A. Jostsons, C.K.H. Dubose, J. Nucl. Mater. 44 (1972) 91.
[6] A. Jostsons, C.K.H. Dubose, G.L. Copeland, J.O. Stiegler, J. Nucl. Mater. 49 (1973/4) 136.
[7] G.W. Hollenberg, W.V. Cummings, J. Am. Ceram. Soc. 60 (1977) 520.
[8] Takako Donomae, Yoshiaki Tachi, Manabu Sekine, Yuko. Morohashi, Naoaki Akasaka, J. Ceram. Soc. Jpn. 115 (2007) 551.
[9] T. Stoto, J. Ardonceau, L. Zuppiroli, Radiat. Eff. 105 (1987) 17.
[10] Tadashi Maruyama, Masaru Iwanami, Somei Ohnuki, Takanori Suda, Seiichi Watanabe and Kazuhiro Ikezawa, Effects of Radiation on Materials: 21st International Symposium, ASTM STP 1447, 2004.

[11] B.N. Singh, T. Leffers, J. Nucl. Mater. 125 (1984) 287.
[12] M. Vivtoria, W.V. Green, B.N. Singh, T. Feffers, J. Nucl. Mater. 122&123 (1984) 737.
[13] G.L. Copeland, C.K.H. Dubose, R.G. Donnelly, W.R. Martin, J. Nucl. Mater. 43 (1972) 126.
[14] T. Stoto, N. Housseau, L. Zuppiroli, B. Kryger, J. Appl. Phys. 68 (1990) 3198.
[15] F.F. Zhang, L.M. Wang, Microsc. Microanal. (2015) (accepted).
[16] H. Trinkaus, B.N. Singh, J. Nucl. Mater. 323 (2003) 229.
[17] P. Dauben, R.P. Wahi, H. Wollenberger, J. Nucl. Mater. 141–143 (1986) 723.
[18] H. Inui, H. Mori, H. Fujita, Scripta Mater. 22 (1988) 249.
[19] H. Inui, H. Mori, H. Fujita, Acta Metall. 37 (1989) 1337.
[20] H. Inui, H. Mori, T. Sakata, H. Fujita, J. Non-Cryst. Solids 116 (1990) 1.
[21] H. Trinkaus, NATO ASI Series, vol. 279, Plenum, 1991.
[22] H.L. Skriver, N.M. Rosengaard, Phys. Rev. B 46 (1992) 7157.
[23] V.M. Kuznetsov, R.I. Kadyrov, G.E. Rudenskii, J. Mater. Sci. Technol. 14 (1998) 320.
[24] J.M. Zhang, F. Ma, K.W. Xu, Appl. Surf. Sci. 229 (2004) 34.
[25] Q.M. Wei, N. Li, K. Sun, L.M. Wang, Scripta Mater. 63 (2010) 430.
[26] P.D. Edmondson, C.M. Parish, Y. Zhang, A. Hallen, M.K. Miller, Scripta Mater. 65 (2011) 731.
[27] R.S. Nelson, D.J. Mazey, R.S. Barnes, Philos. Mag. 11 (1965) 91.
[28] S.E. Donnelly, R.C. Birtcher, C.W. Allen, Science 296 (2002) 507.
[29] K. Furuya, N. Ishikawa, C.W. Allen, J. Microsc. 194 (1999) 152.

Please cite this article in press as: F. Zhang et al., Scripta Mater. (2015), http://dx.doi.org/10.1016/j.scriptamat.2015.07.011